Cross-correlation of the polarizations of the 21-cm and cosmic microwave backgrounds

Lingyuan Ji,[*] Selim C. Hotinli,[†] and Marc Kamionkowski[‡]

Department of Physics and Astronomy, Johns Hopkins University 3400 North Charles Street, Baltimore, Maryland 21218, USA

(Received 15 March 2022; accepted 8 June 2023; published 26 June 2023)

The polarization of the 21-cm radiation from the epoch of reionization arises from Thomson scattering of 21-cm photons from free electrons and provides information that complements that from the intensity fluctuation. Previous work showed that a direct detection of this signal will be difficult, and hinted that the signal might be enhanced via correlation with other tracers. Here, we discuss the cross-correlation between the cosmic microwave background polarization and the 21-cm polarization. We treat reionization using an analytical model with parameters calibrated by seminumerical simulations. We then derive the cross-correlation angular power spectrum using the total-angular-momentum formalism. We also provide a noise analysis to test against the null hypothesis of no 21-cm polarization. We find that, due to the smallness of the signal, it will be difficult to reject this null hypothesis even with a synergy of ambitious next-generation 21-cm and cosmic microwave background missions.

DOI: 10.1103/PhysRevD.107.123533

I. INTRODUCTION

The redshifted 21-cm line of the hydrogen hyperfine transition provides both a spatially and temporally resolved image of the baryons' growth in inhomogeneity, collapse, heating, and reionization [1–3]. A wide range of cosmological and astrophysical information can be derived from it. Previous work focused primarily on the intensity signal, showing its potential power in constraining fundamental physics [4,5], star and galaxy formation [6], and intergalactic medium [7].

More can be learned from the polarization signal. The dominant contribution to the 21-cm polarization arises in the same way as the polarization of the cosmic microwave background (CMB). In the reionized Universe, the Thomson scattering between of a radiation quadrupole from a free electron generates a linear polarization. This effect has first been explored in Refs. [8,9]. Reference [8] estimates the strength of this signal by assuming a relatively simple model of reionization, and claims that it can be detected by Square Kilometre Array (SKA) with a one-month observation time. Reference [9], with refined reionization modeling via 21CMFAST [10,11], concludes that this signal is smaller than the SKA sensitivity. However, Ref. [9] also points out that the signal may still be detected by cross-correlation with other probes.

In this paper, we discuss the cross-correlation between the 21-cm polarization and the CMB polarization. The CMB polarization, produced also by the Thomson scattering, is generated in roughly two different epochs—one right before recombination, the other after reionization. The latter, as we will show, gains contribution from density perturbations within a certain comoving-wavelength range that also give rise to the 21-cm polarization. This generates a cross-correlation. By correlating the well-established CMB signal with a to-be-detected signal, we enhance the sensitivity to the target signal.

To assess the prospects to detect this cross-correlation, we evaluate the ability of future measurements to answer two related but subtly different questions. In the first, we determine the possibility to rule out the null hypothesis of no reionization from this cross-correlation alone. In the second, we assume that reionization has been well established from the CMB-polarization measurement and ask whether the cross-correlation can be detected under this assumption. Of course, the null hypothesis of no reioinization in the first calculation is inconsistent with observations and so this calculation is of academic interest only. We include it, though, to illustrate some of the nuance in the final conclusion that the signal is not detectable. We conclude that the amplitude of the cross-correlation is large enough to distinguish it from the null hypothesis of no reionization, but it cannot be detected under the null hypothesis of a well established detection of the reionization in the CMB polarization.

The rest of the paper is organized as follows. In Sec. II, we present the theoretical calculation of the

[*]lingyuan.ji@jhu.edu
[†]shotinl1@jhu.edu
[‡]kamion@jhu.edu

cross-correlation signal. In Sec. III, we analyze the detection prospect of this signal by next-generation CMB and 21-cm observations, while pointing out potential hurdles. We end in Sec. IV with some concluding remarks.

II. THEORY

The physical picture is illustrated schematically in Fig. 1, which shows the observable Universe in comoving coordinates. As described in the figure caption, we start by discussing the remote intensity anisotropy in Sec. II A; we then move to compute the induced linear polarization in Sec. II B. These steps are done for both the CMB polarization and the 21-cm polarization. Next, we use the results from these previous steps to calculate the cross-correlation angular power spectrum in Sec. II C. Finally, we proceed to describe the "bubble model" for the 21-cm fluctuations in Sec. II D, and its correlation with matter fluctuations. We also discuss how the bubble-model parameters are calibrated to seminumerical simulations using 21CMFAST.

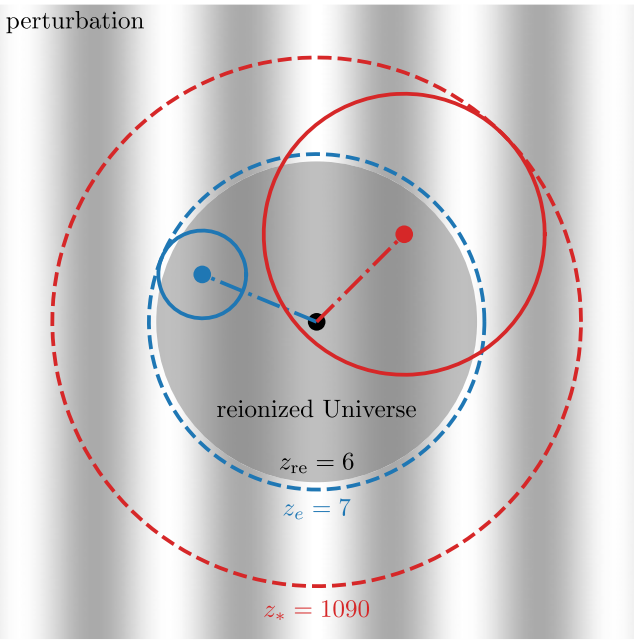

FIG. 1. A comoving-space sketch of the physics described in Sec. II. The observer is located at the central black point. The blue dashed ring represents the emission shell of the 21-cm photons for the *observer*. The reionized Universe (gray disk) contains free electrons. One electron (blue point) sees an intensity anisotropy, resulting from the perturbations (gray plane-wave pattern) at the *electron's* emission shell of the 21-cm photons (solid blue ring). This then produces a linear polarization seen by the observer (along the blue dot-dashed line). Note that the electron's emission shell is different from, but tangent to, that of the observer's. The similar mechanism for the CMB polarization is depicted using the corresponding red elements, while the dashed and the solid rings should be interpreted as the last-scattering surfaces seen by the observer and the electron, respectively. This sketch is drawn *to scale* according to the labeled redshifts.

A. Intensity quadrupole

We first discuss the 21-cm-intensity quadrupole. Here, for simplicity, we take the postheating limit, where the spin temperature T_S is very large compared to the temperature T_γ of the CMB photons, and neglect the effect of redshift-space distortion. Under these assumptions, the differential brightness temperature T_{21} of the redshifted 21-cm line is then proportional to the neutral-hydrogen density $n_{\rm HI}$ at the hydrogen-photon interaction. Since the Thomson scattering is achromatic, it suffices to only account for the fractional perturbation $\delta_{21} \equiv T_{21}/\bar{T}_{21} - 1$, where $\bar{T}_{21}$ is the spatial average of T_{21}.

Since the Thomson scattering is achromatic, the linear polarization of a given frequency ν_o we observe is *only* due to the scattering of those 21-cm photons emitted at redshift $z_e = \nu_e/\nu_o - 1$, and is *independent* of the redshift of the scattering. Here, $\nu_e = 1420$ MHz is the proper frequency of the hydrogen line. Thus the relevant intensity-anisotropy pattern (i.e. responsible for the observed polarization at frequency ν_o) seen by an electron at $(\vec{x}, \eta)$ from direction $\hat{u}$ is

$$\Theta_{21,\nu_o}(\hat{u}; \vec{x}, \eta) \equiv \delta_{21}[\vec{x} + (\eta - \eta_e)\hat{u}, \eta_e], \tag{1}$$

where η_e is the conformal time at redshift z_e. We define the quadrupole tensor

$$t_{ab}^{21,\nu_o}(\vec{x}, \eta) \equiv \int d^2\hat{u}(3u_a u_b - \delta_{ab})\Theta_{21,\nu_o}(\hat{u}; \vec{x}, \eta). \tag{2}$$

It will be useful later to express t_{ab}^{21,ν_o} using δ_{21} in the Fourier space. With detailed derivation given in Appendix A, we write the result here,

$$\tilde{t}_{ab}^{21,\nu_o}(\vec{k}, \eta) = -12\pi j_2[k(\eta - \eta_e)]\left(\hat{k}_a\hat{k}_b - \frac{\delta_{ab}}{3}\right)\tilde{\delta}_{21}(\vec{k}, \eta_e). \tag{3}$$

Here, $j_n(x)$ is the spherical Bessel function; δ_{ab} is the Kronecker delta symbol; $k \equiv |\vec{k}|$ and $\hat{k} \equiv \vec{k}/k$ are the magnitude and direction of the wave vector $\vec{k}$.

Next, we discuss the CMB intensity quadrupole. The polarization of CMB is generated both right before recombination and after reionization. However, only the latter contributes significantly to the cross-correlation with the 21-cm polarization. To see this, we note that, for a given free electron, the intensity quadrupole—thus the resulting polarization—is dominated by perturbations with a wavelength roughly the size of the electron's last-scattering-surface radius. For those free electrons right before recombination, this size is roughly the duration $\Delta\chi_* \sim 15$ Mpc of

recombination (assuming recombination at $z_* = 1090$ with a duration of $\Delta z_* = 80$). So, the recombination polarization pattern will peak at multipole $l \sim \chi_*/\Delta\chi_* \sim 10^3$, where $\chi_* \sim 1.4 \times 10^4$ Mpc is the comoving distance to the last-scattering surface. At these high multipoles, the Limber approximation [12] implies that the 21-cm polarization, coming from a comoving distance different from χ_*, will have very limited correlation with the recombination CMB polarization.

The relevant CMB intensity quadrupole, seen by the free electrons in the reionized Universe, can then be approximated by the Sachs-Wolfe effect. Similar to the 21-cm case, the intensity-anisotropy pattern,

$$\Theta_{\rm CMB}(\hat{u};\vec{x},\eta) \equiv -\frac{1}{3}\Phi[\vec{x} + (\eta - \eta_*)\hat{u}, \eta_*], \tag{4}$$

determines the quadrupole tensor

$$t^{\rm CMB}_{ab}(\vec{x},\eta) \equiv \int d^2\hat{u}(3u_a u_b - \delta_{ab})\Theta_{\rm CMB}(\hat{u};\vec{x},\eta). \tag{5}$$

Here, Φ is the conformal-Newtonian-gauge gravitational potential, and η_* is the conformal time at recombination. This relation can be written in Fourier space, following the derivation in Appendix A, as

$$\tilde{t}^{\rm CMB}_{ab}(\vec{k},\eta) = 4\pi j_2[k(\eta - \eta_*)]\left(\hat{k}_a\hat{k}_b - \frac{\delta_{ab}}{3}\right)\tilde{\Phi}(\vec{k},\eta_*). \tag{6}$$

We can re-express this equation in terms of the matter-density perturbation δ at conformal time η_e by realizing that

$$\tilde{\Phi}(\vec{k},\eta) = \frac{3H_0^2\Omega_m}{2k^2 a(\eta)}\tilde{\delta}(\vec{k},\eta) \tag{7}$$

is constant deep in the matter-dominated era, giving [13]

$$\tilde{t}^{\rm CMB}_{ab}(\vec{k},\eta) = \frac{6\pi H_0^2\Omega_m}{k^2 a(\eta_e)} j_2[k(\eta - \eta_*)]\left(\hat{k}_a\hat{k}_b - \frac{\delta_{ab}}{3}\right)\tilde{\delta}(\vec{k},\eta_e). \tag{8}$$

Here, H_0 is the current Hubble parameter; Ω_m is the matter-density parameter; $a(\eta)$ is the scale factor at conformal time η. We formally switch the time slice from η_* to η_e, so that we only need to refer to the equal-time correlation between δ and δ_{21} at the conformal time η_e of the 21-cm emission.

B. Polarization

The linear polarization tensor, as a function of position $\hat{n}$ on the sky, is

$$P_{AB}(\hat{n}) \equiv \frac{1}{\sqrt{2}}\begin{pmatrix} Q(\hat{n}) & U(\hat{n})\sin\theta \\ U(\hat{n})\sin\theta & -Q(\hat{n})\sin^2\theta \end{pmatrix}, \tag{9}$$

where, $Q(\hat{n})$ and $U(\hat{n})$ are the Stokes parameters measured in the local coordinate frame $\{\hat{\theta},\hat{\phi}\}$. The components of P_{AB} are given in the coordinate chart $\{\theta,\phi\}$, indicated by the capital subscripts AB. The $\sin\theta$-related factors follow from the fact that the chart $\{\theta,\phi\}$ is orthogonal but not orthonormal. Later, we will mainly use the *Cartesian* components P_{ab} of this polarization tensor, which can be obtained by embedding the unit sphere into the three-dimensional space and performing a general coordinate transformation between $\{\theta,\phi\}$ and $\{x,y,z\}$. In both representations, the polarization tensor is symmetric ($P_{AB} = P_{BA}$ and $P_{ab} = P_{ba}$) and trace free ($g^{AB}P_{AB} = 0$ and $g^{ab}P_{ab} = 0$, with $g_{AB} = \mathrm{diag}\{1, \sin^2\theta\}$ and $g_{ab} = \delta_{ab}$). The embedding also implies that P_{ab} is transverse ($\hat{n}_a P_{ab} = 0$).

Both the CMB and the 21-cm polarization are produced by Thomson scattering between free electrons and unpolarized incident radiation possessing a quadrupolar intensity anisotropy. This indicates that, for the probe $X = $ CMB or $21(\nu_o)$, we have

$$P^X_{ab}(\hat{n}) = \frac{\sqrt{2}}{16\pi}\int g(\eta)d\eta\Pi_{ab,ij}(\hat{n})t^X_{ij}[\hat{n}(\eta_0 - \eta), \eta], \tag{10}$$

where the integral starts from η_* for $X = $ CMB and η_e for $X = 21(\nu_o)$, to the current conformal time η_0, and will be omitted from now on. Here, $g(\eta) \equiv e^{-\tau}d\tau/d\eta$ is the photon-visibility function, where the Thomson-scattering optical depth is defined as

$$\tau(\eta) \equiv \int_\eta^{\eta_0} \frac{\sigma_T n_b x_e(\eta')}{a(\eta')^2}d\eta'. \tag{11}$$

Here, σ_T is the total cross section of Thomson scattering, n_b is the *comoving* number density of baryons (which is equal to the current physical number density), and $x_e(\eta)$ is the mean ionization fraction [see Eq. (34)]. Note that $\sigma_T n_b = 2.307 \times 10^{-5}(\Omega_b h^2)$ Mpc^{-1} in terms of the baryon-density parameter Ω_b. The tensor projector is

$$\Pi_{ab,ij}(\hat{n}) \equiv \mathcal{P}_{ai}(\hat{n})\mathcal{P}_{bj}(\hat{n}) - \frac{1}{2}\mathcal{P}_{ij}(\hat{n})\mathcal{P}_{ab}(\hat{n}), \tag{12}$$

where $\mathcal{P}_{ij}(\hat{n}) \equiv \delta_{ij} - \hat{n}_i\hat{n}_j$. Equation (10) must take this form because the integrand is the only possible way to project a three-dimensional quadrupole tensor t_{ij} to a polarization tensor P_{ab} that is simultaneously symmetric, trace free, and transverse. The prefactor in Eq. (10) can be determined by taking $\hat{n} = -\hat{z}$ and comparing to Eq. (2.10) in Ref. [14].

We emphasize that here we compute the large-angle polarization signal, and ignore the effect of patchy reionization on polarization generation through Thomson scattering. Thus, in Eq. (10), the photon-visibility function $g(\eta)$ is taken to be independent of the direction. In Sec. II D,

however, we do consider patchy reionization that gives rise to the 21-cm-intensity anisotropy, since that is crucial in the generation of 21-cm polarization.

C. Angular power spectrum

The statistical property of $P^X_{ab}(\hat{n})$ is encoded in the angular power spectrum $C^{XY}_J \equiv \langle (P^X_{JM})^* P^Y_{JM} \rangle$, where the E-mode spherical-harmonic expansion coefficients are defined as

$$P^X_{JM} \equiv \int d^2\hat{n} [Y^{\rm TE}_{(JM)ab}(\hat{n})]^* P^X_{ab}(\hat{n}), \tag{13}$$

using the tensor spherical harmonics $Y^{\rm TE}_{(JM)ab}(\hat{n})$ defined in Ref. [15]. There exists another family of B-mode expansion coefficients, obtained by projection onto $Y^{\rm TB}_{(JM)ab}(\hat{n})$ (defined also in Ref. [15]), that will be zero under our assumption of no primordial gravitational waves.

The next step is to plug Eq. (10) into Eq. (13) and calculate the angular power spectrum. This task is immensely simplified by the use of total-angular-momentum (TAM) waves defined in Ref. [15], whose notation we shall now follow. Assuming only primordial scalar perturbation, the symmetric and trace-free tensor t^X_{ab} can be expanded as

$$t^X_{ab}(\vec{x},\eta) = \sum_{kJM} t^X_{kJM}(\eta) [4\pi i^J \Psi^{k,{\rm L}}_{(JM)ab}(\vec{x})] \tag{14}$$

in terms of the L-mode tensor TAM waves. Here, $\sum_k$ is a shorthand for $\int k^2 dk/(2\pi)^3$. The projection in Eq. (10) is then simplified by the property

$$\Pi_{ab,ij}(\hat{x}) \Psi^{k,{\rm L}}_{(JM)ij}(\vec{x}) = R^{\rm L,TE}_J(kx) Y^{\rm TE}_{(JM)ab}(\hat{x}) \tag{15}$$

of the TAM waves. Here the radial function $R^{\rm L,TE}_J(kx)$ can be inferred from Eq. (38) of Ref. [16]. It will also be helpful to expand the matter-density perturbation δ and the 21-cm-temperature perturbation δ_{21} in terms of the scalar TAM waves. To simplify the writing of parallel equations, we formally rename

$$\delta_{\rm CMB}(\vec{x},\eta) = \delta(\vec{x},\eta) \quad \text{and} \quad \delta_{21,\nu_o}(\vec{x},\eta) = \delta_{21}(\vec{x},\eta), \tag{16}$$

and exclusively refer to the symbols on the left-hand sides when we abstractly express the probe using X and Y. Now, the expansions can be compactly written as

$$\delta_X(\vec{x},\eta) = \sum_{kJM} \delta^X_{kJM}(\eta) [4\pi i^J \Psi^k_{(JM)}(\vec{x})]. \tag{17}$$

Similar to the Fourier-space relations, Eqs. (3) and (8), t^X_{kJM} can also be related to δ^X_{kJM}. With details given in Appendix B, we list the result here,

$$t^X_{kJM}(\eta) = \mathcal{T}_X(k;\eta,\eta_e) \delta^X_{kJM}(\eta_e). \tag{18}$$

Here the quadrupole transfer functions $\mathcal{T}_X$ are defined as

$$\mathcal{T}_{21,\nu_o}(k;\eta,\eta_e) \equiv 4\pi\sqrt{6} j_2[k(\eta-\eta_e)], \tag{19}$$

$$\mathcal{T}_{\rm CMB}(k;\eta,\eta_e) \equiv -\frac{2\pi\sqrt{6}\Omega_m H_0^2}{k^2 a(\eta_e)} j_2[k(\eta-\eta_*)]. \tag{20}$$

With this setup, we can plug Eq. (18) into Eq. (14), and then the result into Eq. (10) with the aid of Eq. (15). Finally, the orthonormality of $Y^{\rm TE}_{(JM)ab}(\hat{n})$ implies that

$$P^X_{JM} = \frac{\sqrt{2}}{4} i^J \int \frac{k^2 dk}{(2\pi)^3} \mathcal{I}^X_J(k;\eta_e) \delta^X_{kJM}(\eta_e), \tag{21}$$

where the polarization transfer functions $\mathcal{I}^X_J$ (not to be confused with $\mathcal{T}_X$) are defined as

$$\mathcal{I}^X_J(k;\eta_e) \equiv \int g(\eta) d\eta R^{\rm L,TE}_J[k(\eta_0-\eta)] \mathcal{T}_X(k;\eta,\eta_e). \tag{22}$$

The angular power spectrum then evaluates to

$$C^{XY}_J = \frac{1}{8} \int \frac{k^2 dk}{(2\pi)^3} P_{XY}(k;\eta_e) \mathcal{I}^X_J(k;\eta_e) \mathcal{I}^Y_J(k;\eta_e), \tag{23}$$

where the power spectrum is defined such that the products of the TAM coefficients have the expectation values

$$\langle [\delta^X_{kJM}(\eta_e)]^* \delta^Y_{k'J'M'}(\eta_e) \rangle = \delta_{kk'} \delta_{JJ'} \delta_{MM'} P_{XY}(k;\eta_e). \tag{24}$$

Here $\delta_{kk'}$ is a shorthand for $(2\pi)^3 \delta(k-k')/k^2$. Note that this definition coincides with the canonical definition using Fourier coefficients, as detailed in Ref. [15],

$$\langle \tilde{\delta}^*_X(\vec{k},\eta_e) \tilde{\delta}_Y(\vec{k}',\eta_e) \rangle = (2\pi)^3 \delta(\vec{k}-\vec{k}') P_{XY}(k;\eta_e). \tag{25}$$

D. Reionization model

The question now reduces to obtaining P_{XY}, the cross- and auto-spectrum of the matter-density perturbation δ and the 21-cm-temperature perturbation δ_{21}. We employ a simple but effective "bubble model" provided in Ref. [17], with its parameters calibrated to seminumerical simulations via 21CMFAST. We emphasize that here we are, in a sense, only using the bubble model as a fitting template of the simulation results, so we avoid interpreting the fitted values of the model parameters in a physical way. This approach is similar to that used in Ref. [9] (i.e. assuming a specific bias scaling outside the k range of the simulation).

Reference [17] models the ionization-fraction field via a collection of (possibly overlapping) fully ionized bubbles.

The bubbles are biased tracers of the underlying matter-density field, and have a log-normal radius R distribution $P(R)$,

$$P(R) = \frac{1}{R\sigma_{\ln R}\sqrt{2\pi}} \exp\left[-\frac{(\ln R - \mu_{\ln R})^2}{2\sigma^2_{\ln R}}\right], \quad (26)$$

where $\mu_{\ln R}$ and $\sigma_{\ln R}$ are the mean and the standard deviation of $\ln R$, respectively. Note that the mean bubble radius is then $\langle R\rangle = \exp(\mu_{\ln R} + \sigma^2_{\ln R}/2)$.

The 21-cm-temperature perturbation, in the limit detailed in Sec. II A, becomes $\delta_{21} \equiv n_{\rm HI}/\bar{n}_{\rm HI} - 1$. The bubble model then predicts[1] its autospectrum

$$P_{\delta_{21},\delta_{21}} = [b\langle W_R(k)\rangle \ln(1-x_e) + 1]^2 P_{\delta\delta} + \frac{x_e}{1-x_e}[\langle V_b\rangle\langle W_R^2(k)\rangle + \tilde{P}_{\delta\delta}], \quad (27)$$

and its cross-spectrum with matter-density perturbation

$$P_{\delta_{21},\delta} = [b\langle W_R(k)\rangle \ln(1-x_e) + 1]P_{\delta\delta}. \quad (28)$$

In those equations, we define the mean bubble volume

$$\langle V_b\rangle \equiv \int P(R) dR V_b(R), \quad (29)$$

where $V_b(R) \equiv 4\pi R^3/3$ is the volume of single bubble with radius R. We also define the volume-weighted window function as

$$\langle W_R^n(k)\rangle \equiv \frac{1}{\langle V_b\rangle^n}\int P(R) dR V_b^n(R) W_R^n(k) (n = 1,2), \quad (30)$$

where $W_R(k) = 3[\sin(kR) - kR\cos(kR)]/(kR)^3$ is the spherical top hat window function in the Fourier space. In addition, we define

$$\tilde{P}_{\delta\delta} \equiv \frac{P_{\delta\delta}\langle V_b\rangle\langle\sigma_R^2\rangle}{\sqrt{P_{\delta\delta}^2 + \langle V_b\rangle^2\langle\sigma_R^2\rangle^2}}, \quad (31)$$

where $P_{\delta\delta}$ is the matter power spectrum, and

$$\langle\sigma_R^2\rangle \equiv \frac{1}{\langle V_b\rangle^2}\int P(R) dR V_b^2(R)\sigma_R^2 \quad (32)$$

is the volume-weighted average of

$$\sigma_R^2 \equiv \int \frac{dk}{k} W_R^2(k)\frac{k^3}{2\pi^2} P_{\delta\delta}(k), \quad (33)$$

which is the variance of the mean fluctuation in a spherical region of radius R. Equations (27) and (28), plus the matter power spectrum $P_{\delta\delta}$ can then be used to compute the angular power spectrum via Eq. (23). We model the redshift evolution of the mean ionization fraction x_e with a hyperbolic tangent as

$$x_e(z) = \frac{1}{2}\left\{1 - \tanh\left[\frac{y(z) - y_{\rm re}}{\Delta_y}\right]\right\}, \quad (34)$$

where Δ_y and $y_{\rm re}$ are model parameters and $y(z) = (1+z)^{3/2}$. We illustrate the results of our bubble-model calculation—whose parameters are chosen to match the seminumerical 21CMFAST simulations—in Fig. 2, together with the results from simulations, for a set of redshifts where the signal-to-noise ratio of the effect is highest. In order to match the redshift evolution of the mean ionization fraction, we have chosen $y_{\rm re} = 25.6$ and $\Delta_y = 4.9$, which match well to the simulations at $z < 7.2$.

III. FORECAST

Here, we assess the detectability of the cross-correlation signal between the 21-cm polarization and the CMB. Upcoming 21-cm power-spectrum experiments, such as HERA [18] and SKA1-low [19,20], will generate a wealth of high-precision data in the following years. These experiments are primarily designed as interferometers and the bulk of the scientific effort in modeling the involved systematics focuses on increasing the measurement quality on scales relevant to the baryon-acoustic oscillations, $0.1\ h/\text{Mpc} < k < 1.0\ h/\text{Mpc}$. These radio interferometers are limited on large scales, however, by their minimum dish (or antenna) separation. This sets a limit on the minimum ℓ multipole that can be measured. The anticipated designs of HERA and SKA experimental configurations suggest that multipoles lower that ∼10 will not be accessible when operated as interferometers. Nevertheless, experiments like HERA can also be operated in a single-dish mode, allowing a solution to this problem (see e.g. [21]).

Another cause for concern is the observational systematics, which includes the beam profile, the $1/f$ noise, and the foreground wedge [22–24] of the 21-cm experiment at hand. These have been primarily studied in the context of interferometer experiments. Encouragingly, however, phase-1 experiments like MeerKAT[2] (an SKA precursor on the planned site of SKA1-MID [25]) are already taking data, albeit on low redshifts $z < 3$. Nevertheless,

[1]Note that Ref. [17] predicts spectra involving $\delta_{\rm HI} \equiv (n_{\rm HI} - \bar{n}_{\rm HI})/\bar{n}_{\rm H}$, which is normalized differently from $\delta_{21} \equiv n_{\rm HI}/\bar{n}_{\rm HI} - 1$ interested in here. The conversion is $\delta_{21} = \delta_{\rm HI}/(1-x_e)$. Here, Eqs. (27) and (28) have already been adjusted with appropriate powers of $(1-x_e)$.

[2]www.sarao.ac.za.

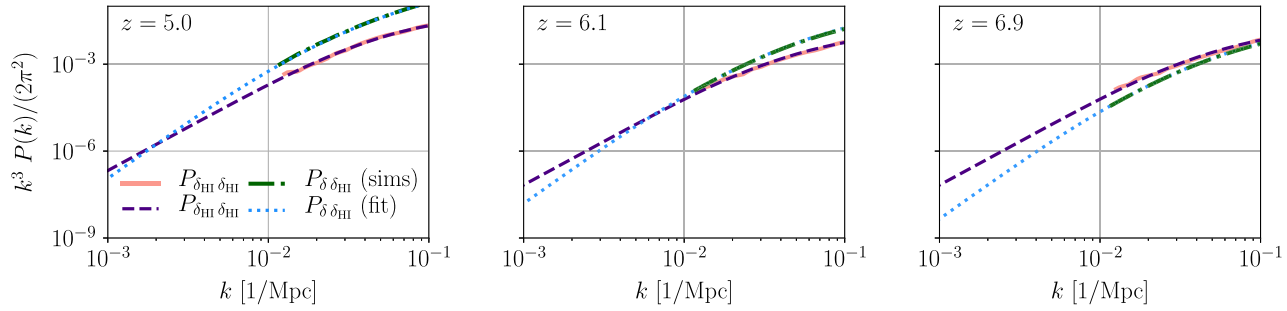

FIG. 2. The anticipated auto- and cross-correlation signals from neutral-hydrogen and density fluctuations. The light-red (purple) solid (dashed) lines correspond to auto-correlation power-spectra of the neutral hydrogen fluctuations. The green (blue) dot-dashed (dotted) lines correspond to cross-correlation of the hydrogen and the density perturbations. We extrapolate the results from the seminumerical 21CMFAST code to larger scales with the bubble model, introduced in Sec. II. We use the *Planck* 2019 cosmological parameters and the Λ cold dark matter model for the matter power spectra and fit the bubble-model parameters to the simulations. Solid and dot-dashed lines show our results from simulations while dashed and dotted lines are our results from the fits. We show the spectra at three redshift values, $z \in \{5.0, 6.1, 6.8\}$, which dominate the signal-to-noise in our analysis in Sec. III.

overcoming these systematic challenges should be equally plausible for intensity mapping at higher redshifts. It is not difficult to imagine that path-finder experiments like MeerKAT will provide the road map for using HERA (or similar precision) experiments in single-dish mode when measuring the epoch of reionization.

Finally, it is possible for the 21-cm polarization measurements to suffer unique (and major) challenges in addition to intensity. These include calibration [26–28], foregrounds from polarized synchrotron emission [29–31], instrumental leakage of intensity into polarization [32], Faraday rotation from various sources of magnetic fields [33–35] and depolarization effects [36,37]. While there is ongoing research concerning these systematics, their effective mitigation may be challenging for the near-future surveys. Nevertheless, since these effects are not correlated with the CMB data, the cross-correlation signal that we study in this work should be less susceptible to systematics and may prove a promising direction forward.

In what follows we model the anticipated noise (per multipole) from a single-dish 21-cm power-spectrum measurement as [38–40]

$$N_\ell^{E_{21}(z)} = \frac{\Omega_{\rm pix} T_{\rm sys}^2}{B t_{\rm o} \bar{T}_b^2} \exp\{\ell(\ell+1)(\theta_B\sqrt{8\ln 2})^2\}, \quad (35)$$

where $\theta_B = \lambda/D_{\rm dish}$ is the beam full-width at half-maximum of a single dish with diameter $D_{\rm dish}$ at wavelength $\lambda = \lambda_{21}(1+z)$, $\Omega_{\rm pix} = 1.13\theta_B^2$ for a Gaussian beam, $T_{\rm sys}$ is the system temperature, $B(z)$ is the frequency bandwidth of observation, $t_{\rm o}$ is the total observation time and $\bar{T}_b(z)$ is the measured mean baryonic temperature at redshift z. We ignore the so-called foreground wedge (see e.g. [41]) since, in principle, foregrounds do not lead to a loss of information (a similar approach is taken in e.g. Ref. [42]), and the wedge can potentially be removed with better understanding of the instrument [43,44]. We demonstrate the anticipated noise on the 21-cm polarization in Fig. 3 along with the anticipated polarization signals from the CMB and 21-cm and the CMB intensity noise for *Planck*.

We define the detection signal-to-noise (SNR) of the cross-correlation as

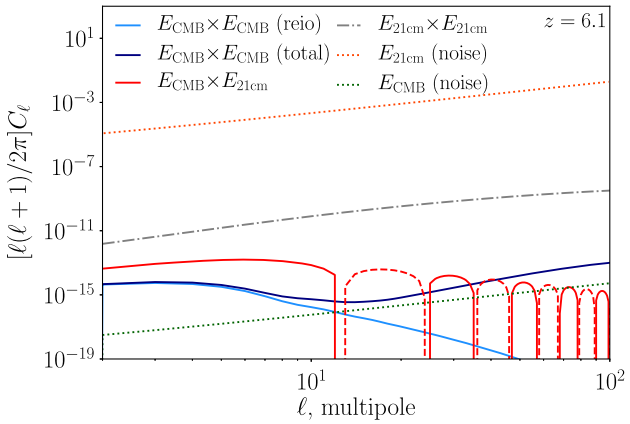

FIG. 3. CMB polarization spectrum, the anticipated polarization autocorrelation from reionization and the anticipated cross-correlation between the CMB polarization and the 21 cm. Solid dark blue line is the total CMB signal, including the reionization bump, latter shown with light blue solid line. The dot-dashed gray line is the autocorrelation of the 21-cm polarization. The red solid line is the cross-correlation signal where the negative values are shown with the red dashed line. The dotted orange line is the anticipated 21-cm polarization noise for the fiducial experiment we consider, as described in Sec. III. The green dotted line is the Planck instrument noise. The 21-cm signal and noise were calculated at redshift $z = 6.1$ and for a redshift bin of size $\Delta z = 1$. We have taken $\Delta_T = 1$ μK-arcmin for demonstration. All spectra shown here are dimensionless (normalized to the sky-average intensities of the corresponding probes, see Sec. II).

$$\mathrm{SNR}^2 = \sum_{n_f \ell \ell'} C_\ell^{E_{\rm CMB} E_{21}} \mathbf{cov}^{-1}(\tilde{C}_\ell^{E_{\rm CMB} E_{21}}, \tilde{C}_{\ell'}^{E_{\rm CMB} E_{21}}) C_{\ell'}^{E_{\rm CMB} E_{21}}, \tag{36}$$

where

$$\mathbf{cov}\left(\tilde{C}_\ell^{E_{\rm CMB} E_{21}}, \tilde{C}_{\ell'}^{E_{\rm CMB} E_{21}}\right) = \frac{\delta_{\ell\ell'} f_{\rm sky}^{-1}}{2\ell+1}\left(\tilde{C}_\ell^{E_{\rm CMB} E_{\rm CMB}} \tilde{C}_\ell^{E_{21} E_{21}} + C_\ell^{E_{\rm CMB} E_{21}} C_\ell^{E_{\rm CMB} E_{21}}\right). \tag{37}$$

Here, n_f varies over the multiple frequency bands for the 21-cm observations,[3] $f_{\rm sky}$ is the sky fraction, $C_\ell^{E_{\rm CMB} E_{21}}$ is the cross-correlation between the CMB polarization and the 21-cm polarization, $C_\ell^{E_{\rm CMB} E_{\rm CMB}}$ and $C_\ell^{E_{21} E_{21}}$ are the auto-correlations of the CMB and 21-cm polarization, respectively, and spectra denoted with tildes are observed values, i.e. $\tilde{C}_\ell = C_\ell + N_\ell$. In Eqs. (36) and (37) we omitted showing the redshift (or frequency) dependence of the signals explicitly for brevity. In this analysis we take six frequency bands covering the range $4 < z < 16$.

In what follows, we test two hypotheses. First, to access the detectability of the polarization cross-correlation signal between 21-cm and CMB, we take a null hypothesis scenario in which there is no reionization bump signal in the CMB autocorrelation in the covariance of Eq. (36) and exclude the cosmic variance from the 21-cm polarization autocorrelation. We also take the noise and signal to be diagonal in redshift bins and no signal or noise in the cross-correlation signal in the covariance of Eq. (36). Second, we ask this: "*knowing that there is indeed a period of reionization, would we see the 21-cm-CMB E mode correlation?*" For the latter, we include the reionization bump signal in the CMB autocorrelation cosmic variance. We emphasize, however, that the first hypothesis underestimates the variance of the cross-correlation, thus overestimating the SNR, *if the knowledge of reionization is estabiliahed through other means*. In our Universe, we have this knowledge, and thus should quote the SNR computed in the second hypothesis as the forecast.

We consider a fiducial 21-cm experiment with $T_{\rm sys} = 40$ K and satisfying $\theta_B(z) = 20$ arcmin at $z = 6.1$. We take five redshift bins in the range $z \in [4, 11]$ with redshift depth $\Delta z = 1$, and model the CMB noise as $N_\ell^{EE} = 2(\Delta_T/T_{\gamma,0})^2 \exp\{\ell(\ell+1)\theta_{\rm FWHM}^2/8\ln 2\}$, where $\theta_{\rm FWHM}$ is the beam size of the CMB experiment, satisfying $\theta_{\rm FWHM} \simeq 5$ arcmin for *Planck*, and $T_{\gamma,0}$ is the current CMB temperature. For our first hypothesis, we find such an experiment can reach detection SNR $= 2.1$ with a dedicated 2 years of observation over the full sky, if cross-correlated with a CMB experiment with thermal noise $\Delta_T = 1$ μK-arcmin with the *Planck*-sized $\theta_{\rm FWHM} \simeq 5$ arcmin beam. Note that this thermal noise for the CMB experiment is lower than *Planck*. While upcoming CMB experiments such as SO and CMB-S4 will lower the thermal noise on small scales significantly, improving the fidelity of large-scale measurements ($\ell < 30$) requires satellite experiments that do not suffer the atmospheric noise. A promising next-generation experiment was proposed in Ref. [45], which may play a crucial role in measuring the cross-correlation signal we study in this paper. For the null hypothesis the SNR depends on survey specifications as

$$\mathrm{SNR} \simeq 2.1 f_{\rm sky}\left(\frac{20'}{\theta_B^*}\right)^2\left(\frac{1\ \mu\mathrm{K}'}{\Delta_T}\right)^2\left(\frac{40\ \mathrm{K}}{T_{\rm sys}}\right)^2 \frac{t_0}{2\ \mathrm{yrs}}, \tag{38}$$

where θ_B^* is the beam at $z_* = 6.1$. Here, we have taken the minimum multipole as $\ell_{\rm min} = 2$. For our second hypothesis, we find the coefficient of Eq. (38) degrade by over an order of magnitude to SNR $\simeq 0.017$ due to the large cosmic variance of the reionization bump. For the first hypothesis, we find that the SNR depends on the choice of $\ell_{\rm min}$ as SNR $\propto \exp\{-4\ell_{\rm min}/5\}$, suggesting that the measurement of the largest scales will be crucial for detection. We find the decrease with increasing multipoles is less rapid for the second hypothesis, where the SNR depends on choice of $\ell_{\rm min}$ as SNR $\propto \exp\{-0.3\ell_{\rm min}\}$. Since reaching any of these specifications remains challenging for the near-future experiments, we conclude detecting the cross-correlation signal will be difficult, but not impossible with dedicated next-generation surveys.

IV. CONCLUSION

In this paper, we propose to enhance the detectability of the 21-cm polarization by cross-correlation with the CMB polarization. We present the theoretical procedure to compute this cross-correlation from reionization physics, which is then modeled by the bubble model with parameters calibrated to the simulation results of 21CMFAST. We demonstrate the prospect of detection by performing a basic noise analysis, and give the SNR as a function of observational parameters.

In the noise analysis, we choose to test two closely related, but subtly different, null hypotheses. In the first scenario, we assume that there is no reionization, and subsequently no 21-cm or reionization-era CMB polarization. In the second scenario, we assume that there is no 21-cm polarization, but the reionization-era CMB polarization is present. In each scenario, we forecast how strongly will the null hypotheses be disfavored by the observation of 21-cm-CMB polarization correlation.

[3]Note the 21-cm cross power between different frequency bands in practice affects the SNR on large scales if a finer binning in frequencies compared to what we consider here is applied; in which case it should be taken into account in the analysis.

We find that, with very generous assumptions on the 21-cm observational systematics, the synergy of ambitious next-generation 21-cm and CMB missions could make a detection in the first scenario, while the second scenario will still remain out of reach. In the first scenario, the observation at large angular scales is crucial, as that is where the correlation gains most of its contribution.

Future work could improve on the reionization modeling with larger numerical simulations, include the effect of redshift-space distortion, discuss the 21-cm-radiation field before the saturation of heating, provide a more realistic account for the 21-cm observational systematics, and devise strategies to mitigate foregrounds unique to the 21-cm polarization measurement, especially the Faraday rotation induced by the magnetic fields.

ACKNOWLEDGMENTS

This work was supported by NSF Grant No. 2112699 and the Simons Foundation. This work was performed in part at Aspen Center for Physics, which is supported by National Science Foundation Grant No. PHY-1607611, and was partially supported by a grant from the Simons Foundation. S. C. H. is supported by the Horizon Fellowship from Johns Hopkins University.

APPENDIX A: DERIVATION OF THE QUADRUPOLE TENSOR AND ITS TAM COEFICIENTS

When the observed anisotropy at $(\vec{x},\eta)$ is determined by the value of some field ϕ on the emission shell $\vec{x}_e \equiv \vec{x} + (\eta-\eta_e)\hat{u}$ at conformal time η_e,

$$\Theta(\hat{u},\vec{x},\eta) = \phi[\vec{x}+(\eta-\eta_e)\hat{u},\eta_e], \tag{A1}$$

the associated quadrupole tensor is

$$t_{ab}(\vec{x},\eta) \equiv \int d^2u(3u_au_b-\delta_{ab})\phi[\vec{x}+(\eta-\eta_e)\hat{u},\eta_e]. \tag{A2}$$

In Fourier space, this relation takes the form

$$\begin{aligned}\tilde{t}_{ab}(\vec{k},\eta) &= \int d^2u(3u_au_b-\delta_{ab})\int d^3x\exp(-i\vec{k}\cdot\vec{x}) \\ &\quad\times\phi[\vec{x}+(\eta-\eta_e)\hat{u},\eta_e], \\ &= \tilde{\phi}(\vec{k},\eta_e)\int d^2u(3u_au_b-\delta_{ab})\exp[i\vec{k}\cdot\hat{u}(\eta-\eta_e)], \\ &= -12\pi j_2[k(\eta-\eta_e)]\left(\hat{k}_a\hat{k}_b-\frac{\delta_{ab}}{3}\right)\tilde{\phi}(\vec{k},\eta_e).\end{aligned} \tag{A3}$$

Here, in the second equal sign, we have used the shift formula of the Fourier transform. In the third equal sign, the integral can be evaluate by taking $\vec{k}=k\hat{z}$, and then be restored to its general form via symmetry.

APPENDIX B: TRANSFER FUNCTIONS

Equations (8) and (104) of Ref. [15] can convert the Fourier amplitudes to the TAM coefficients, giving

$$t_{kJM}(\eta) = 4\pi\sqrt{6}j_2[k(\eta-\eta_e)]\phi_{kJM}(\eta_e). \tag{B1}$$

For the 21-cm signal and the CMB, let ϕ be δ_{21} and $-\Phi/3$, respectively. We have

$$t^{21,\nu_o}_{kJM}(\eta) = \mathcal{T}_{21,\nu_o}(k;\eta,\eta_e)\delta^{21}_{kJM}(\eta_e), \tag{B2}$$

$$t^{\mathrm{CMB}}_{kJM}(\eta) = \mathcal{T}_{\mathrm{CMB}}(k;\eta,\eta_e)\delta_{kJM}(\eta_e), \tag{B3}$$

where

$$\mathcal{T}_{21,\nu_o}(k;\eta,\eta_e) = 4\pi\sqrt{6}j_2[k(\eta-\eta_e)], \tag{B4}$$

$$\mathcal{T}_{\mathrm{CMB}}(k;\eta,\eta_e) = -\frac{2\pi\sqrt{6}\Omega_mH_0^2}{k^2a(\eta_e)}j_2[k(\eta-\eta_*)]. \tag{B5}$$

In the second formula we used the relation $\tilde{\Phi}(\vec{k},\eta) = 3\Omega_mH_0^2\tilde{\delta}(\vec{k},\eta)/[2k^2a(\eta)]$ and the fact that $\tilde{\Phi}(\vec{k},\eta)$ is approximately constant deep in the matter-dominated era.

[1] J. R. Pritchard and A. Loeb, 21-cm cosmology in the 21st century, Rep. Prog. Phys. **75**, 086901 (2012).
[2] S. Furlanetto, S. P. Oh, and F. Briggs, Cosmology at low frequencies: The 21 cm transition and the High-Redshift Universe, Phys. Rep. **433**, 181 (2006).
[3] M. F. Morales and J. S. B. Wyithe, Reionization and cosmology with 21 cm fluctuations, Annu. Rev. Astron. Astrophys. **48**, 127 (2010).
[4] A. Weltman, P. Bull, S. Camera, K. Kelley, H. Padmanabhan, J. Pritchard, A. Raccanelli, S. Riemer-Sørensen, L. Shao, S. Andrianomena *et al.*, Fundamental physics with the Square Kilometre Array, Pub. Astron. Soc. Aust. **37**, e002 (2020).
[5] R. Ansari *et al.* (Cosmic Visions 21 cm), Inflation and early dark energy with a stage II hydrogen intensity mapping experiment, arXiv:1810.09572.

[6] G. Mellema, L. V. E. Koopmans, F. A. Abdalla, G. Bernardi, B. Ciardi, S. Daiboo, A. G. de Bruyn, K. K. Datta, H. Falcke, A. Ferrara *et al.*, Reionization and the cosmic dawn with the Square Kilometre Array, Exp. Astron. **36**, 235 (2013).
[7] X. H. Fan, C. L. Carilli, and B. G. Keating, Observational constraints on cosmic reionization, Annu. Rev. Astron. Astrophys. **44**, 415 (2006).
[8] D. Babich and A. Loeb, Polarization of 21 cm radiation from the epoch of reionization, Astrophys. J. **635**, 1 (2005).
[9] B. Li, J. Tan, and Y. Mao, Linear polarization of the 21 cm line from the epoch of reionization, Astrophys. J. **918**, 14 (2021).
[10] S. G. Murray, B. Greig, A. Mesinger, J. B. Muñoz, Y. Qin, J. Park, and C. A. Watkinson, 21 cmFAST v3: A PYTHON-integrated C code for generating 3D realizations of the cosmic 21 cm signal, J. Open Source Softwaare **5**, 2582 (2020).
[11] A. Mesinger, S. Furlanetto, and R. Cen, 21 cmFAST: A fast, semi-numerical simulation of the high-redshift 21-cm signal, Mon. Not. R. Astron. Soc. **411**, 955 (2011).
[12] P. Lemos, A. Challinor, and G. Efstathiou, The effect of limber and flat-sky approximations on galaxy weak lensing, J. Cosmol. Astropart. Phys. 05 (2017) 014.
[13] L. Ji, M. Kamionkowski, and K. Inomata, Standard model prediction for cosmological 21 cm circular polarization, Phys. Rev. D **103**, 023516 (2021).
[14] A. Kosowsky, Cosmic microwave background polarization, Ann. Phys. (Paris) **246**, 49 (1996).
[15] L. Dai, M. Kamionkowski, and D. Jeong, Total angular momentum waves for scalar, vector, and tensor fields, Phys. Rev. D **86**, 125013 (2012).
[16] K. Inomata and M. Kamionkowski, Circular polarization of the cosmic microwave background from vector and tensor perturbations, Phys. Rev. D **99**, 043501 (2019).
[17] X. Wang and W. Hu, Redshift space 21 cm power spectra from reionization, Astrophys. J. **643**, 585 (2006).
[18] D. R. DeBoer, A. R. Parsons, J. E. Aguirre, P. Alexander, Z. S. Ali, A. P. Beardsley, G. Bernardi, J. D. Bowman, R. F. Bradley, C. L. Carilli *et al.*, Hydrogen Epoch of Reionization Array (HERA), Publ. Astron. Soc. Pac. **129**, 045001 (2017).
[19] R. Braun, A. Bonaldi, T. Bourke, E. Keane, and J. Wagg, Anticipated performance of the Square Kilometre Array: Phase 1 (SKA1), arXiv:1912.12699.
[20] D. J. Bacon *et al.* (SKA Collaboration), Cosmology with phase 1 of the Square Kilometre Array: Red book 2018: Technical specifications and performance forecasts, Pub. Astron. Soc. Aust. **37**, e007 (2020).
[21] P. Bull, P. G. Ferreira, P. Patel, and M. G. Santos, Late-time cosmology with 21 cm intensity mapping experiments, Astrophys. J. **803**, 21 (2015).
[22] A. R. Parsons, J. C. Pober, J. E. Aguirre, C. L. Carilli, D. C. Jacobs, and D. F. Moore, A per-baseline, delay-spectrum technique for accessing the 21 cm cosmic reionization signature, Astrophys. J. **756**, 165 (2012).
[23] A. Liu, A. R. Parsons, and C. M. Trott, Epoch of reionization window. I. Mathematical formalism, Phys. Rev. D **90**, 023018 (2014).
[24] A. Liu, A. R. Parsons, and C. M. Trott, Epoch of reionization window. II. Statistical methods for foreground wedge reduction, Phys. Rev. D **90**, 023019 (2014).
[25] R. S. Booth, W. J. G. de Blok, J. L. Jonas, and B. Fanaroff, MeerKAT key project science, specifications, and proposals, arXiv:0910.2935.
[26] J. P. Hamaker, J. P. Bregman, and R. J. Sault, Understanding radio polarimetry. I. Mathematical foundations, Astron. Astrophys. Suppl. Ser. **117**, 137 (1996).
[27] G. Bernardi, L. J. Greenhill, D. A. Mitchell, S. M. Ord, B. J. Hazelton, B. M. Gaensler, A. de Oliveira-Costa, M. F. Morales, R. U. Shankar, R. Subrahmanyan *et al.*, A 189 MHz, 2400 square degree polarization survey with the Murchison Widefield Array 32-element prototype, Astrophys. J. **771**, 105 (2013).
[28] S. A. Kohn, J. E. Aguirre, P. La Plante *et al.*, The HERA-19 Commissioning Array: Direction-dependent effects, Astrophys. J. **882**, 58 (2019).
[29] L. Page *et al.* (WMAP Collaboration), Three year Wilkinson Microwave Anisotropy Probe (WMAP) observations: Polarization analysis, Astrophys. J. Suppl. Ser. **170**, 335 (2007).
[30] E. Lenc, B. M. Gaensler, X. H. Sun *et al.*, Low-frequency observations of linearly polarized structures in the interstellar medium near the south galactic pole, Astrophys. J. **830**, 38 (2016).
[31] C. L. Van Eck, M. Haverkorn, M. I. R. Alves *et al.*, Diffuse polarized emission in the LOFAR Two-meter Sky Survey, Astron. Astrophys. **623**, A71 (2019).
[32] K. M. B. Asad, L. V. E. Koopmans, V. Jelić, A. G. de Bruyn, V. N. Pandey, and B. K. Gehlot, Polarization leakage in epoch of reionization windows: III. Wide-field effects of narrow-field arrays, Mon. Not. R. Astron. Soc. **476**, 3051 (2018).
[33] V. Jelic, S. Zaroubi, P. Labropoulos, G. Bernardi, A. G. de Bruyn, and L. V. E. Koopmans, Realistic simulations of the galactic polarized foreground: Consequences for 21-cm reionization detection experiments, Mon. Not. R. Astron. Soc. **409**, 1647 (2010).
[34] O. M. Smirnov, Revisiting the radio interferometer measurement equation. IV. A generalized tensor formalism, Astron. Astrophys. **531**, A159 (2011).
[35] D. F. Moore, J. E. Aguirre, A. R. Parsons, D. C. Jacobs, and J. C. Pober, The effects of polarized foregrounds on 21 cm epoch of reionization power spectrum measurements, Astrophys. J. **769**, 154 (2013).
[36] B. J. Burn, On the depolarization of discrete radio sources by Faraday dispersion, Mon. Not. R. Astron. Soc. **133**, 67 (1966).
[37] L. Pratley and M. Johnston-Hollitt, Wide-band rotation measure synthesis, Astrophys. J. **894**, 38 (2020).
[38] R. A. Battye, I. W. A. Browne, C. Dickinson, G. Heron, B. Maffei, and A. Pourtsidou, HI intensity mapping: A single dish approach, Mon. Not. R. Astron. Soc. **434**, 1239 (2013).
[39] A. Pourtsidou, D. Bacon, R. Crittenden, and R. B. Metcalf, Prospects for clustering and lensing measurements with forthcoming intensity mapping and optical surveys, Mon. Not. R. Astron. Soc. **459**, 863 (2016).
[40] A. Pourtsidou, D. Bacon, and R. Crittenden, HI and cosmological constraints from intensity mapping, optical

and CMB surveys, Mon. Not. R. Astron. Soc. **470**, 4251 (2017).

[41] J. C. Pober, A. R. Parsons, D. R. DeBoer, P. McDonald, M. McQuinn, J. E. Aguirre, Z. Ali, R. F. Bradley, T. C. Chang, and M. F. Morales, The baryon acoustic oscillation broadband and broad-beam array: Design overview and sensitivity forecasts, Astron. J. **145**, 65 (2013).

[42] D. Li, H. M. Zhu, and U. L. Pen, Cross-correlation of the kinematic Sunyaev-Zel'dovich effect and 21 cm intensity mapping with tidal reconstruction, Phys. Rev. D **100**, 023517 (2019).

[43] S. Gagnon-Hartman, Y. Cui, A. Liu, and S. Ravanbakhsh, Recovering the wedge modes lost to 21-cm foregrounds, Mon. Not. R. Astron. Soc. **504**, 4716 (2021).

[44] A. Liu, Y. Zhang, and A. R. Parsons, Spherical harmonic analyses of intensity mapping power spectra, Astrophys. J. **833**, 242 (2016).

[45] K. Basu, M. Remazeilles, J. B. Melin, D. Alonso, J. G. Bartlett, N. Battaglia, J. Chluba, E. Churazov, J. Delabrouille, J. Erler *et al.*, A space mission to map the entire observable universe using the CMB as a backlight: Voyage 2050 science white paper, Exp. Astron. **51**, 1555 (2021).